

VIOLATION OF SYNCHROTRON LINE OF DEATH BY THE HIGHLY POLARIZED GRB 160802A

VIKAS CHAND

Tata Institute of Fundamental Research, Mumbai, India

TANMOY CHATTOPADHYAY

Pennsylvania State University, State College, PA, USA

S. IYYANI

The Inter-University Centre for Astronomy and Astrophysics, Pune, India

RUPAL BASAK

The Oskar Klein Centre for Cosmoparticle Physics, AlbaNova, SE-106 91 Stockholm, Sweden; Department of Physics, KTH Royal Institute of Technology, AlbaNova University Center, SE-106 91 Stockholm, Sweden

AARTHY, E.

Physical Research Laboratory, Ahmedabad, Gujarat, India

A. R. RAO

Tata Institute of Fundamental Research, Mumbai, India

SANTOSH V. VADAWALE

Physical Research Laboratory, Ahmedabad, Gujarat, India

DIPANKAR BHATTACHARYA

The Inter-University Centre for Astronomy and Astrophysics, Pune, India

V. B. BHALERAO

Indian Institute of Technology, Bombay, India

ABSTRACT

GRB 160802A is one of the brightest gamma-ray bursts (GRBs) observed with *Fermi* Gamma-ray Burst Monitor (GBM) in the energy range of 10–1000 keV, while at the same time it is surprisingly faint at energies $\gtrsim 2$ MeV. An observation with *AstroSat*/CZT Imager (CZTI) also provides the polarisation which helps in constraining different prompt emission models using the novel joint spectra-polarimetric data. We analyze the *Fermi*/GBM data, and find two main bursting episodes that are clearly separated in time, one particularly faint in higher energies and having certain differences in their spectra. The spectrum in general shows a hard-to-soft evolution in both the episodes. Only the later part of the first episode shows intensity tracking behaviour corresponding to multiple pulses. The photon index of the spectrum is hard, and in over 90 per cent cases, cross even the slow cooling limit ($\alpha = -2/3$) of an optically thin synchrotron shock model (SSM). Though such hard values are generally associated with a sub-dominant thermal emission, such a component is not statistically required in our analysis. In addition, the measured polarisation in 100–300 keV is too high, $\pi = 85 \pm 29\%$, to be accommodated in such a scenario. Jitter radiation, which allows a much harder index up to $\alpha = +0.5$, in principle can produce high polarisation but only beyond the spectral peak, which in our case lies close to 200–300 keV during the time when most of the polarisation signal is obtained. The spectro-polarimetric data seems to be consistent with a subphotospheric dissipation process occurring within a narrow jet with a sharp drop in emissivity beyond the jet edge, and viewed along its boundary.

Keywords: gamma-ray burst: general – gamma-ray burst: individual (GRB160802A) – polarization –

radiation mechanisms: non-thermal

1. INTRODUCTION

One of the putative models invoked to explain the non-thermal spectral shape in the prompt emission of gamma-ray bursts (GRB) is the synchrotron shock model (SSM). In this model, electrons gyrating in the magnetic field at internal shocks generate synchrotron photons that are observed at gamma ray energies, boosted by the relativistic bulk motion of the jet (Rees & Meszaros 1992, Meszaros & Rees 1993, Rees & Meszaros 1994). One of the predictions of the SSM is the so-called ‘‘synchrotron line of death (LOD)’’. The low energy photon spectral index should not exceed the value $-2/3$ for an optically thin shocked material. If the effects of the synchrotron cooling are also taken into consideration (Katz 1994, Sari et al. 1996, Sari & Piran 1997), then the index can lie in the range of $-3/2$ to $-2/3$. The distribution of the indices was, however, found to violate these limits (Cohen et al. 1997, Crider et al. 1997, Preece et al. 1998, Ghirlanda et al. 2003).

The measurement of the low energy spectral index, however, depends on the spectral modelling of the GRB prompt emission. For most of the GRBs the shape of the spectrum could be phenomenologically well described by a Band function (Band et al. 1993), which consists of two smoothly joined power law functions. The model parameters are low and high energy indices (α and β), the energy where the νF_ν spectrum peaks (E_p) and the normalization. Besides this empirical model, GRBs are known to show the evidence of other components in the prompt emission spectrum. These include one or more thermal components modeled as a blackbody (Ryde 2005; Page et al. 2011, Guiriec et al. 2011, Guiriec et al. 2013, Guiriec et al. 2015a, Basak & Rao 2015) or a non-thermal component modeled by a power law or cut-off power law extending up to high energies (>100 MeV) that is observed in Fermi LAT energy band (González et al. 2003, Abdo et al. 2009, Ackermann et al. 2013). In a unified model for prompt emission from optical to γ -rays, deviation from Band model is fit by a three-component model which includes two non-thermal components and a thermal component (Guiriec et al. 2015b, Guiriec et al. 2016, Guiriec et al. 2015a).

Some studies show that the spectral evolution of a single emission component can sometimes make Band + BB artificially fit the data significantly better than Band alone if the integration time is too long. Thus for an unambiguous detection of the thermal component, it is generally necessary to verify the presence of the thermal component in time resolved spectra as well (Burgess & Ryde 2015). Hence, though the inclusion of thermal component can alleviate the problem of line of death (LOD)

violation, we must be cautious of such cases. In addition, Burgess et al. (2015) have used a physical synchrotron model with a blackbody and found that the problem of LOD violation persists in many cases. They have also found a more severe LOD $\alpha \sim -0.8$ and pointed out the need for some other emission mechanisms. One such proposed mechanism is Jitter radiation. These radiations are emitted by ultra relativistic electrons in a non-uniform, small-scale magnetic field and produces a spectral shape that is different from the synchrotron radiation (Medvedev 2000). The allowed photon index in a Jitter radiation can reach up to $+0.5$.

From data analysis point of view, GRBs with high signal to noise spectral data are ideal to try out different emission models as the prompt emission shows rapid spectral evolution and these GRBs provide good enough signal for time resolved studies. However, the spectral and timing data so far have not been able to pin down the radiation mechanism. It is thus very important to study bright GRBs with well defined spectral shapes using other informations such as X-ray polarisation during the prompt emission phase. As different emission models predict different degree of polarisation in different energy bands, this is a powerful technique to provide strong constraints on the possible models. GRB 160802A is a bright GRB showing significant hard X-ray polarization (Chattopadhyay et al. 2017). It shows two pulses in its lightcurve and the spectrum is well fit by a simple Band function and hence it offers a very good opportunity to carry out a simultaneous timing, spectral and polarisation study of a class of GRBs violating LOD.

In Section 2 we discuss the joint usage of Fermi and *AstroSat* for spectral and polarization studies of GRBs. Then we present the timing and spectral properties of the GRB in Section 3. We conclude and discuss our results in Section 4.

2. FERMI AND ASTROSAT DATA

For many years, *Neil Gehrels Swift Observatory* and *Fermi* satellites have been providing detailed information on the prompt emission of GRBs (Gehrels & Razzaque 2013). The Burst Alert Telescope (BAT) on-board Swift (Gehrels et al. 2004) is a dedicated instrument to detect GRBs and the satellite slews and points towards the location of a GRB during the prompt emission. BAT, however, has a relatively narrow energy band and hence the spectrum of the prompt emission for the BAT detected GRBs can be generally modeled as a simple powerlaw. Gamma-Ray Burst Monitor (GBM) on board *Fermi* is comprised of 12 sodium iodide (NaI) detectors and 2 bismuth germanate (BGO) detectors (Meegan et al. 2009). These detectors are sensitive in the 8

keV – 1 MeV and 150 keV – 40 MeV energy range, respectively. In addition, the Large Area Telescope (LAT) on board *Fermi*, is sensitive from 20 MeV to 300 GeV (Atwood et al. 2009). The unprecedented coverage over seven decades in energy by *Fermi* has led to the discovery of substantially new science for GRBs. The *Fermi*/LAT GRB catalog contains several interesting bright bursts and *Fermi* helped revealing a new spectral component that exists up to GeV energies or spectral breaks existing in the MeV energy ranges (Abdo et al. 2009, Izzo et al. 2012, Ackermann et al. 2010, Vianello et al. 2017, Wang et al. 2017). Still it is generally felt that the spectral modelling alone is unable to solve the problem of radiation mechanism of the GRB prompt emission due to various issues. Some key problems are e.g., (a) the same data can be fit with a variety of models and the true model cannot be determined based on the goodness of fit; (b) even if the best-fit model is determined, the models are generally phenomenological and may not conform with the underlying theory e.g., the LOD violation; (c) sometimes an additional spectral component e.g., a blackbody may change the parameters of the other component e.g., Band function in such a way that it conforms with the underlying model, but the additional component is not statistically required. A critical component that can break these degeneracies inherent in spectral modelling is the measurement of X-ray polarisation. The Cadmium Zinc Telluride Imager (CZTI) on board *AstroSat* is highly sensitive to hard X-ray polarisation (Chattopadhyay et al. 2014, Vadawale et al. 2015, see also Section 4 of Chattopadhyay et al. 2017).

AstroSat is a multi-wavelength observatory which was launched on 2015 September 28 (Singh et al. 2014). The CZTI focal plane consists of pixellated detectors sensitive in the energy range of 20-200 keV, with sensitivity gradually falling off till about 500 keV. All CZTI data are acquired in “event mode”, with individual photons time-tagged at 20 μ s resolution (Bhalerao et al. 2017). CZTI can help the study of GRB prompt emission by measuring X-ray polarization in the 100 - 300 keV range (Chattopadhyay et al. 2014; Vadawale et al. 2015). The photons preferentially scattered in the direction perpendicular to the polarization direction, give rise to an asymmetry/modulation in an otherwise flat azimuthal angle distribution. Amplitude of the modulation is directly proportional to the polarization fraction embedded in the incident radiation. Selection procedure of the Compton events in CZTI is discussed in detail in Chattopadhyay et al. (2014).

The spectral and temporal properties from *Fermi* and polarization from the *AstroSat*/CZTI can give a complete information about a GRB. We need to study these gathered information individually as well as a statistical sample of it. GRB 160802A is one of the GRBs observed

in both *Fermi* and *AstroSat*/CZTI. We present here a combined temporal, spectral, and polarization characteristics of this GRB.

3. GRB 160802A

3.1. Observations

GRB 160802A was detected by *Fermi*/GBM at UT 06:13:29.63 (Bissaldi 2016) as a very bright GRB with two peaks, and a T_{90} of 16.4 ± 0.4 s in the 50–300 keV band (see Kouveliotou et al. 1993 for a definition of T_{90}). Both the peaks showed a Fast Rise Exponential Decay (FRED)-like profile. The peak energy of the Band function fit to the time-integrated spectrum ($T_0 - 0.3$ s to $T_0 + 19.4$ s) is 284 ± 7 keV in the preliminary analysis. The fluence as observed in the 10-1000 keV band is $1.04 \pm 0.08 \times 10^{-4}$ erg cm^{-2} . *AstroSat*/CZTI data show a complex light curve with $T_{90} = 16.8$ s (Bhalerao et al. 2016). The burst was also detected by several other satellites including the *Block for X-ray and gamma-radiation detection Lomonosov*, *BDRG* (Panasyuk et al. 2016), *Wind/Konus* (Kozlova et al. 2016b) and the *Calorimetric Electron Telescope*, *CALET* (Tamura et al. 2016). No low energy (X-rays, optical, radio etc.) and high energy (GeV) afterglows were reported for GRB 160802A¹.

3.2. Light curves

Lightcurves obtained from NaI and BGO detectors of *Fermi*-GBM clearly show two peaks separated by ~ 8 s in GRB 160802A (Fig. 1). The left panels show lightcurves in different energy bins, plotted at 1 second resolution. Bayesian blocks (Scargle et al. 2013) are obtained using *Fermi science tool gtburstfit* with *ncpprior* parameter set to 9. A fit obtained by Bayesian blocks analysis is overplotted with a solid black line. We see that the second episode is softer: with a high count rate at low energies, but rapidly diminishing above 400 keV. We studied lightcurves with finer energy bands to identify bands with significant emission, and found that at energies $\gtrsim 2$ MeV, any putative signal in BGO is indistinguishable from background. To highlight these features, the right panel of Fig. 1 shows lightcurves with 64 ms time resolution.

3.3. Spectral analysis of the prompt emission

We undertake detailed spectral analysis with data from GBM detectors with the strongest signal: NaI 2 (n2), with the GRB just 20° from its boresight, and NaI a (na), which detected the GRB at an off-axis angle of 54° . We also select the BGO detector closest to the GRB direction (BGO 0). We use *Time-Tagged-Events* (TTE) data

¹ <https://gcn.gsfc.nasa.gov/other/160802A.gcn3>

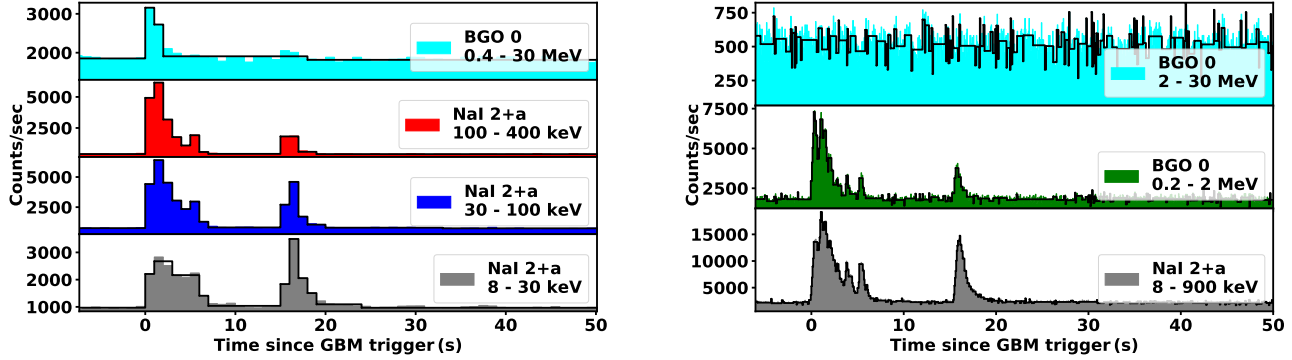


Figure 1: Left: Composite light curve with 1 s resolution showing cumulative rates from two NaI detectors (NaI 2, a) and BGO 0. Bayesian blocks are overplotted and show the light curves obtained using these blocks of constant rate. Right: light curve with a higher temporal resolution of 64 ms. The emission is limited up to energy ~ 2 MeV in the BGO as shown in the top panel.

provided by the GBM team and publicly available on the FSSC² website. We generate custom response matrices and spectrum files using the public software `gtburst`³ and using best localization available interplanetary network (IPN) triangulation (Kozlova et al. 2016a). The response file is a weighted response for an interval split over multiple extensions where each extension contains response for a particular time interval which can vary within extensions. The software `gtburst` assign weights when a selected time-bin for spectral analysis is split across two or multiple extensions. The spectra were analyzed in `XSPEC` (Arnaud 1996). Spectra reduced using `gtburst` are PHA 2 files and can be directly used in `XSPEC` by referencing the spectrum number. Our data are Poissonian in nature, with a Gaussian background derived from modelling the spectrum in intervals before and after the GRB emission. Hence, we use `pgstat`⁴ as the data fit estimator. Effective area corrections were applied among the GBM and BGO detectors and to avoid the k-edge 33-37 keV energy range was excluded for the analysis of NaI data. There is a trade-off between the reduction in `pgstat` and increase in the number of model parameters used to fit the data. This comparison can be made by using the Bayesian Information Criterion (BIC). The BIC can be calculated from the `pgstat` value, the number of free parameters to be estimated (k), and the number of data points (n) as

$$\text{BIC} = -2\ln(L) + k\ln(n)$$

where L is the likelihood of a model for best fit parameters (Schwarz 1995). When written in terms of likelihood

² Fermi Science Support Center, <https://fermi.gsfc.nasa.gov/ssc/>.

³ <https://fermi.gsfc.nasa.gov/ssc/data/analysis/scitools/gtburst.html>

⁴ <https://heasarc.gsfc.nasa.gov/xanadu/xspec/manual/node293.html>

function we can have $pgstat = -2\ln(L)$, where L is the likelihood of a model for best fit parameters (Schwarz 1995). A model yielding a lower BIC as compared to other models is taken to be preferred model, based on the magnitude of the reduction in BIC. A change of $\Delta\text{BIC} \geq 6$ is a strong evidence of improvement (Kass & Raftery 1995). An example of using BIC for distinguishing among different models used to fit the GRB spectrum can be found for the case of GRB 160625B in Wang et al. (2017).

We find that for GRB 160802A, the time-integrated *Fermi* spectrum is best fit by a Band function with $E_p = 276^{+15}_{-14}$ keV, $\alpha = -0.71^{+0.03}_{-0.03}$ and $\beta = -2.5^{+0.1}_{-0.2}$. Here α satisfies the LOD condition, $\alpha < -2/3$. A thermal blackbody component added to the spectrum improves the fit: $\Delta pgstat \sim 16$ ($\Delta\text{BIC} = 3$) for 2 more free parameters, although this is only a hint for the presence of a thermal component and a detailed spectral analysis is further required.

Then we perform a spectral fitting to the two episodes separately using Band and cut-off power-law (CPL) models, with or without a blackbody (BB) component and the results are given in Table 1. We find that for the first episode α of Band-only fit is $-0.52^{+0.04}_{-0.03}$, violating the synchrotron LOD for slow cooling. Addition of a blackbody to the Band function softens the value of α to $-0.73^{+0.06}_{-0.05}$ which is now consistent with the LOD condition. The addition of the blackbody to either Band or CPL model significantly improves the fit for the first episode with $\Delta\text{BIC} = 16$ and 55, respectively. For the second episode the addition of the blackbody component is required only for the CPL model ($\Delta\text{BIC} = 24$), while indeed it is disfavoured in case of Band function with $\Delta\text{BIC} = -6$. The spectra for time-integrated analysis are shown in Figure 2. A blackbody in the integrated spectrum is just a first step towards finding a thermal

component. In order to verify that the added blackbody component is physical and not an artefact of an evolving Band function, we then resort to time resolved spectral analysis.

3.4. Time resolved analysis with coarse bins

We divide the GRB lightcurve into coarse bins corresponding to the Bayesian blocks (BB) obtained from 1 second light-curves (§3.2). The Bayesian blocks algorithm objectively divides the data into an optimum set of blocks with no statistically significant variation from a constant rate within each block (Scargle et al. 2013). The time intervals thus obtained along with the models tested are given in Table 2. The synchrotron LOD is violated in the first three intervals as is evident by the contour maps of α - E_p shown in Figure 3. In the intervals (i), (ii) & (viii), BB added to Band gives equally well fit and for intervals (iv), (vii) and (ix), a powerlaw with sharp break (*XSPEC* model *bknpower*) is at par with Band function. With the addition of a BB, the value of the spectral index α softens in all the time bins. The presence of BB can also be an artefact of the evolution of Band function parameters with time. This can be tested by fitting spectra to smaller time bins, and requiring the smooth evolution of parameters like the blackbody temperature with time (see for instance Guiriec et al. 2011, 2013; Burgess & Ryde 2015). Motivated by the results from coarse analysis, we explore this further in §3.5.

3.5. Detailed time-resolved analysis

The time intervals are obtained by choosing a constant signal to noise ratio (SNR) of 30 in the light curve obtained from NaI detector *n2* (which has the highest observed rates). We found that the addition of a blackbody does not give a smooth evolution of its parameters, the temperature of BB fluctuates erratically and in many bins, it remained unconstrained. Moreover the Band function emerges as the preferred model over BB+Band in all the bins, as evidenced by the increase in BIC values after adding the blackbody component (see Table 3). We conclude that we do not detect any significant blackbody component in the prompt emission of GRB 160802A.

The evolution of the peak energy (E_p) of GRBs has been found to show hard to soft evolution with time in some GRBs, E_p tracks the intensity variations in others, while some GRBs show a mixture of both phenomena (Lu et al. 2012). An exception to this behavior is found in the case of GRB 151006A (Basak et al. 2017) where a hardening (increase) in E_p is found in an apparently single pulse towards the end of the emission. The variation of the spectral parameters along with flux (Figure 4) show the E_p values for the first episode initially follow a hard to soft (HTS) trend, and then track the 8–900 keV flux. In particular, the evolution of E_p is very fast in

the first second: showing an order of magnitude change as it decreases from ~ 1000 keV to 200 keV. The fast evolution is likely to have manifested itself as a curvature in the spectrum, which was incorrectly modeled as a blackbody in the coarse analysis (§3.4).

From the evolution of α we find that the values are crossing the LOD as shown in Figure 4. The results are unaltered if we use only one of the detectors *n2* that has pointing angle $< 50^\circ$. The value of α and E_p are determined by the data below the break energy, while the β is determined from data at the energies above that. Although Fermi GBM covers the whole of the burst, the number of photons are very few at energies in the BGO band. Therefore β remains unconstrained in most of the bins and is manifested as a steep high energy power law component of the Band function (in νF_ν representation) because of large magnitudes of the nominal best-fit values.

3.6. Polarization analysis

Chattopadhyay et al. (2017) made a systematic analysis of the GRBs detected by CZTI during the first year of its operation and have reported positive polarisation detection (chance probability < 0.1) for 5 of the 11 GRBs having sufficient number of Compton events for polarisation analysis. GRB 160802A shows a high degree of polarisation ($85 \pm 30\%$) and it has the second highest Bayes factor for the polarized model as compared to the unpolarized model among all the GRBs. We have explored the polarisation characteristics of this GRB with an aim to optimise the polarisation measurement in terms of the selected energy and time windows.

GRB 160802A shows two distinct peaks and, further, it also shows two distinct phases of spectra in the first peak: the first phase (covering 0 – 2.5 s, see Figure 4) having high E_p and hard low energy spectral index, and the second phase with more modest values of E_p and a softer low energy spectral index. Most of the time E_p is above 200 keV. CZT Imager is sensitive for polarisation in the 100 – 400 keV range, the efficiency peaking at lower energies. Hence, for this analysis we restrict ourselves to the energy range of 110 – 175 keV, consistently below the spectral peak (E_p). To investigate the variation of the polarisation characteristics with the pulse characteristics, we undertook polarisation measurements in three distinct time intervals: (i) $\Delta t < 2.74$ s (measured from the Fermi trigger time), (ii) 2.74 s $< \Delta t < 5.64$ s, and (iii) 15.65 s $< \Delta t < 20.34$ s (second pulse). The results are shown in Figure 5.

It is interesting to note that in spite of a large variation in the flux as well as low energy spectral index, the polarisation value remains high throughout the burst.

4. DISCUSSION AND CONCLUSIONS

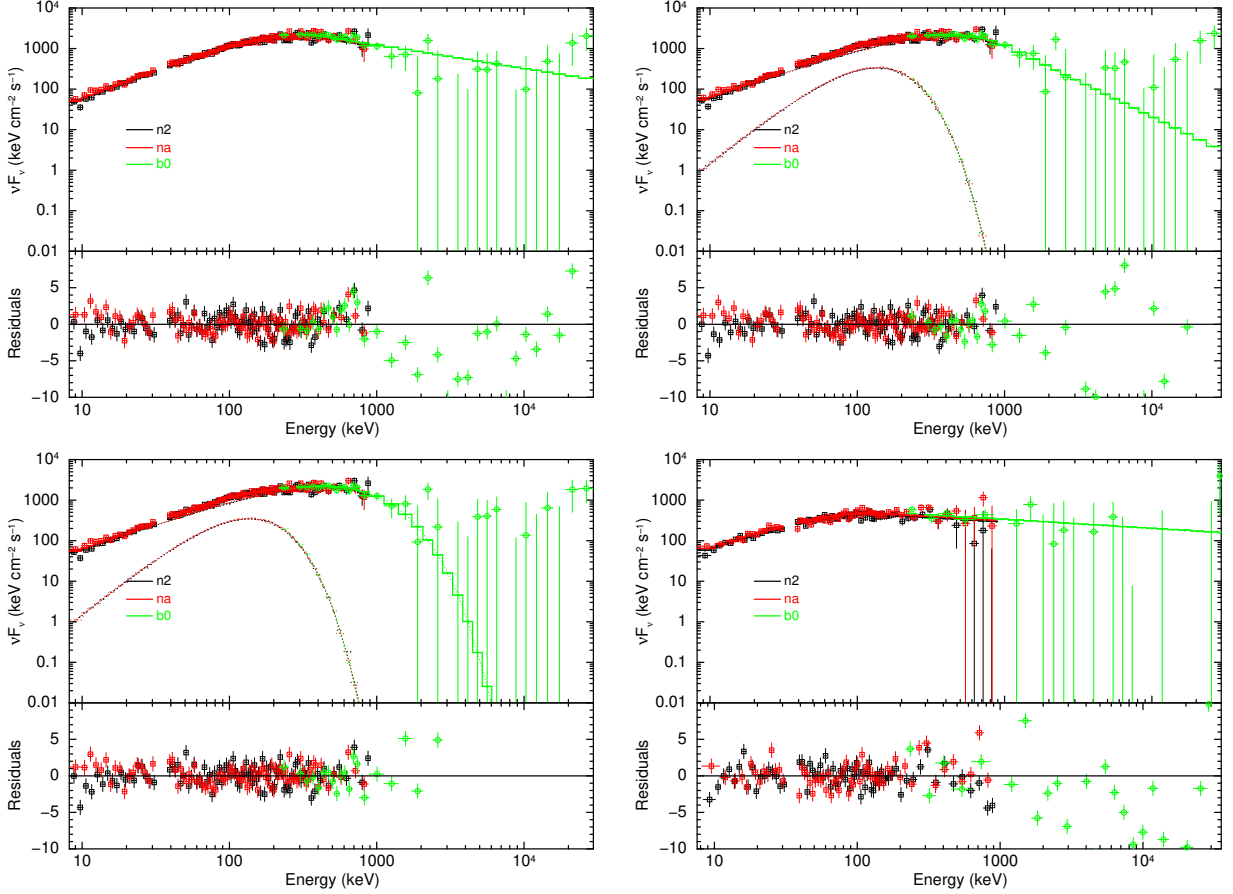


Figure 2: The unfolded time integrated spectrum of GRB 160802A for pulse 1 & 2 are shown along with the residuals (limited between -10 to 10) to the fit. The Band model (top left), an additional blackbody (top right) and blackbody added to a powerlaw with an exponential cut-off (bottom left) are for the pulse 1 and a band function fit (bottom right) is shown for pulse 2.

We have carried out systematic analysis of spectral and polarisation data from *Fermi* and *AstroSat/CZTI* respectively for GRB 160802A. Our analysis derives a number of important constraints as follows.

- (a) We obtain hard α values most of which lie above -0.67 , the line of death of synchrotron emission in slow cooling limit (Cohen et al. 1997; Crider et al. 1997; Ghirlanda et al. 2003; Preece et al. 1998; Goldstein et al. 2013), throughout the burst duration including the first and second episodes (0–7s and 12–20s). In coarse time bins though the spectra show a hint of a Black Body (BB) component, this is most probably an artefact of evolving peak energy (Burgess & Ryde 2015). In the finer resolved time bins, the BB component is never statistically required and α still remains above the line of death (Crider et al. 1997; Preece et al. 1998; Ghirlanda et al. 2003).
- (b) During the initial part of the first pulse α is found to get harder with time, even reaching values > 0 .
- (c) The peak energy E_p in general shows a decreasing trend across each major episodes of emission. However, note that the first episode possesses multiple pulses in the light curve (Fig. 1), in contrast to the second episode which is a smooth single pulse. Thereby, the E_p evolution in the first episode is more complex, starting with a hard-to-soft (HTS) evolution, followed by an intensity tracking behaviour at later times.
- (d) Interestingly, it can also be noted that across the first episode (significantly in the first pulse of the episode), the time evolution of E_{peak} and α have a negative correlation in contrast to what is typically observed in bursts (Kaneko et al. 2006), whereas a positive correlation can be observed in the second episode.
- (e) No high energy emission above 2 MeV is observed which suggests a cutoff above this energy.
- (f) Finally, strong polarisation, $\pi = 85 \pm 29\%$ in energy range 100–175 keV is observed, in both the

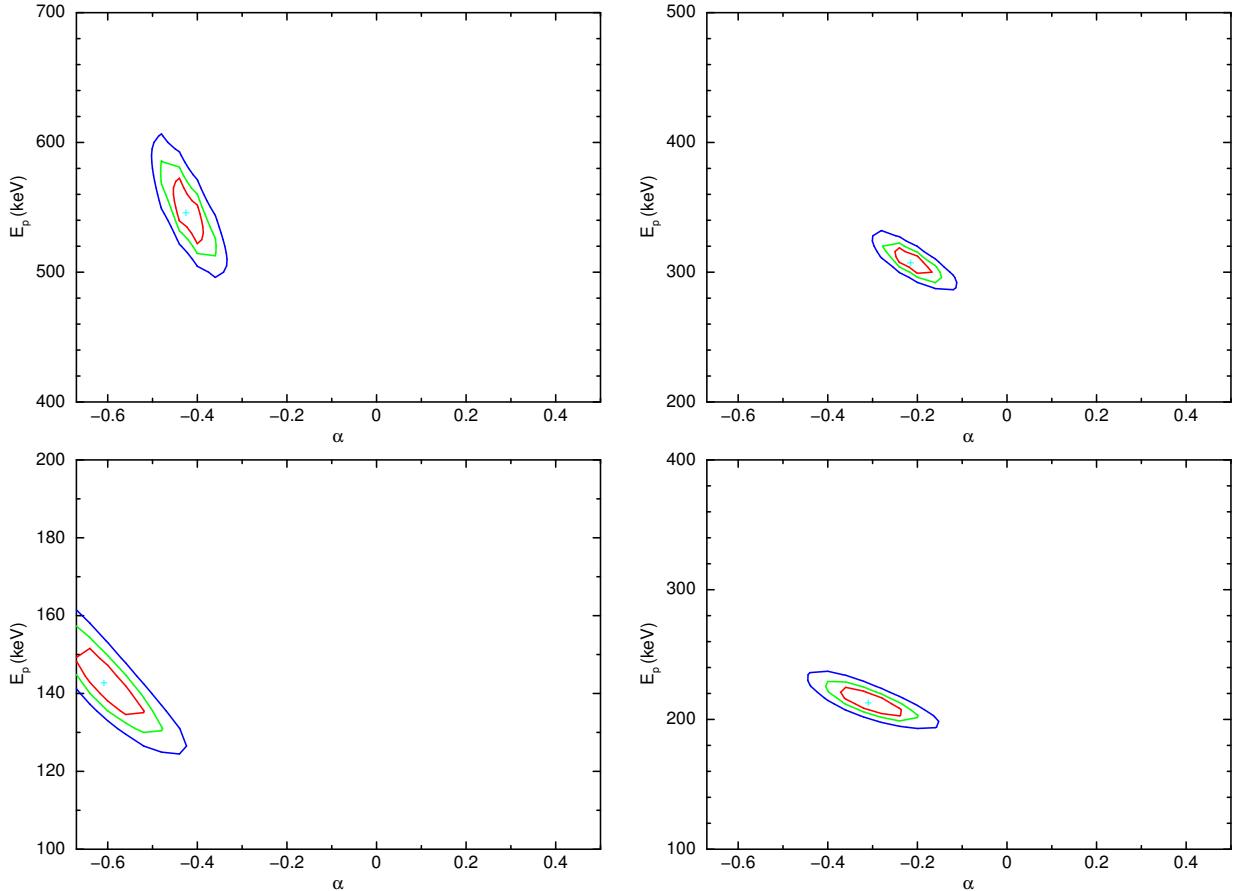


Figure 3: The confidence contours of α and E_p are shown for the coarse time bins (i), (ii), (iii) and (viii) clockwise from the top left. For the first three intervals which spans time interval 0 – 3 s, the value of α is greater than what is expected from the popular SSM. For (viii) however, the α encompasses the allowed value in its 2σ contour. Y-axis (E_p) is drawn at the line of death value $-2/3$.

episodes.

On an average the β of the Band function fit to the spectrum is -3.4 with standard deviation $\langle \sigma \rangle = 1.9$ for the burst (Table 3). This indicates a strong curvature at the high energy end of the spectrum. In such a scenario a negative correlation between E_p and α implies the following: i) The decrease in E_p with time is accompanied by a narrowing of the spectrum. ii) As the E_p values are well constrained and are located well within the energy window, the inferred hardening of α is real, and not an artefact caused by E_p being close to the edge of the observing band. iii) This behaviour also suggests that the overlapping of spectra in each time bin due to time integration is minimum. If significant overlapping of spectra with decreasing E_p did occur, then it would result in an average spectrum with softer α . Also note that in segments of evolution where E_p is not found to be decreasing, the corresponding α values are relatively soft, indicating that such segments may consist of overlap of several pulses Ryde & Svensson (1999).

The obtained hard values of $\alpha > -0.67$ lead to the

inference that the observed spectra are inconsistent with the optically thin fast ($\alpha = -1.5$) and slow cooling ($\alpha = -0.67$) synchrotron emission models (Katz 1994, Rees & Meszaros 1994, Tavani 1996, Sari et al. 1998) as well as with the fast cooling synchrotron emission model from a decaying magnetic field ($\alpha \leq -0.8$) (Uhm & Zhang 2014). A smooth Band function with a hard α may suggest a photospheric emission scenario wherein continuous dissipation occurs at high optical depths extending till the photosphere (Beloborodov 2010). If so, then the spectral peak would be unpolarised as it corresponds to the Wien peak formed at higher optical depths. However, during the interval 1.6 s to 5.64 s post trigger, the E_p lies between 100–300 keV, within the CZTI band where high polarisation is observed. This observation is thus incongruous with the above model. Polarisation imparted by scattering does not help either, since at large optical depths multiple scatterings tend to wash out the directionality. Therefore the observed high polarisation cannot be expected from the subphotospheric dissipation model based on Comptonisation (see Lundman et al.

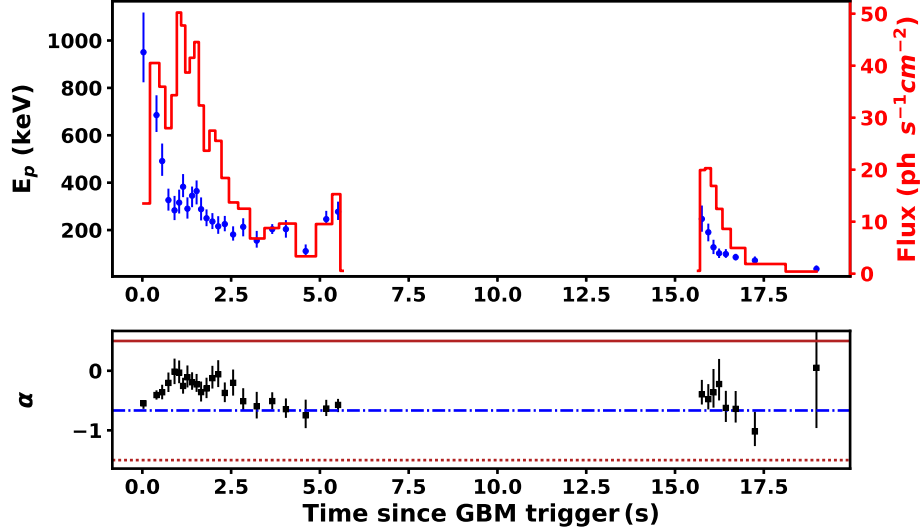


Figure 4: The E_p evolves with time like a hard to soft (HTS) evolution initially and then intensity tracking for the first episode. Second episode has HTS evolution of its E_p . The photon flux calculated in 8 - 1000 keV is also shown in the background. The three horizontal lines in the second panel are lines of death for synchrotron fast cooling ($\alpha = -3/2$, dotted red line), synchrotron slow cooling ($\alpha = -2/3$, blue dash-dot line), and Jitter radiation ($\alpha = +1/2$, solid red line).

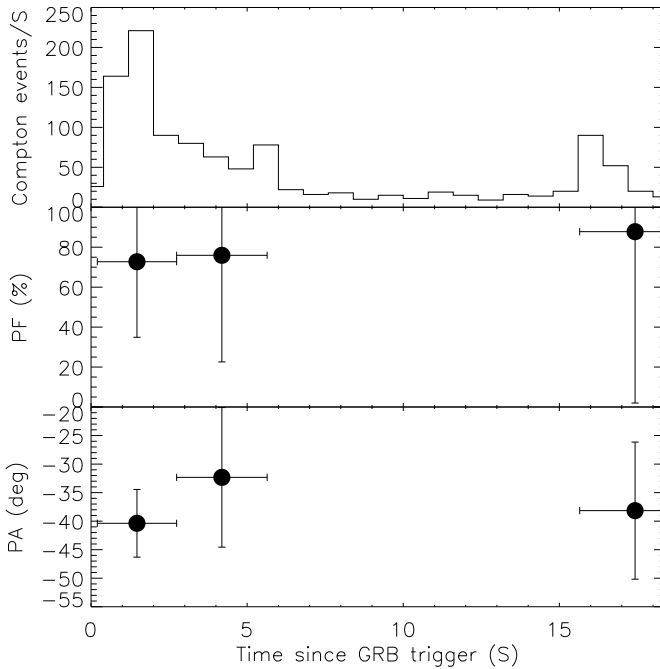


Figure 5: The Compton double events (top panel), polarisation fraction (middle panel) and the polarisation angle (bottom panel) of GRB 160802A as a function of time (§3.6).

2016 for more details).

Another non-thermal process which could be compatible with the observed hard values of α is Jitter radiation (Medvedev 2000), wherein small scale random magnetic turbulence (correlation length, $\lambda_B <$ Larmor radius of the electron) can result in deflection of the electrons on scales less than the beaming angle. The emission thus produced can result in hard spectra ($\alpha > -0.67$) and can in principle be as large as $+0.5$. The Jitter emission spectrum, however, is better modeled by a sharp broken power law instead of a smooth function such as Band function. Jitter radiation, in contrast to synchrotron emission, extends to frequencies well beyond the synchrotron critical frequency: up to $a^3\omega_c$ where $a = R_L/\lambda$, R_L the Larmor radius, λ the characteristic scale of turbulence in the outflow, and ω_c is the characteristic synchrotron frequency. Since $a \gg 1$, emission extending to high energy gamma rays are expected (Aharonian et al. 2002, Kelner et al. 2013). However, here we find a cutoff in emission around 2 MeV. High polarisation in case of Jitter radiation can be achieved only in a specific geometry where the magnetic field turbulence is constrained within a slab (or plane) that is viewed nearly edge on. This can result in polarisation degrees as high as 90% (Prosekin et al. 2016). However, it is important to note that irrespective of the observing angle the degree of polarisation is highest at energies much beyond the spectral peak. Around the spectral peak, the polarisation is expected to be relatively low with values $\leq 40\%$ (see Fig 1 of Prosekin et al. 2016).

Hard α values also suggests that our line of sight is not significantly off the burst axis (Lundman et al. 2013), and that the central engine is active throughout the burst duration. At large off-axis angles and when the central engine is off, the observed emission would be dominated by high latitude emissions, resulting in a softer spectrum both in terms of E_p and α due to lower Doppler boost and superposition of spectra respectively. This would result in an average spectrum with region below the spectral peak $-1 \geq \alpha \geq -0.5$ (Lundman et al. 2013; Pe’er 2008), softer than what is observed here. Both the emission models discussed above, while being capable of generating spectra nearly compatible with those observed, find it difficult to explain the high degree of polarisation around the spectral peak. The observed high polarisation therefore results most likely from the viewing geometry, as envisaged by Waxman (2003), who showed that bright and highly polarised emission can be seen when the observer’s line of sight makes an angle $\theta_j \leq \theta_v \leq \theta_j + 1/\Gamma$ from the jet axis, where θ_j is the jet opening angle, θ_v is the viewing angle with respect to the axis of the jet and Γ is the Lorentz factor of the outflow. This also requires a strong asymmetry in observed emission within the off-axis viewing cone as could be obtained in a “top-hat” jet model, but not in “structured jet” models where emissivity drops slowly away from the jet axis. A sharp drop in emissivity beyond the edge of the jet is also suggested by the observed hard α values. In case of structured jets, the emission viewed off-axis would be dominated by that from high latitudes, resulting in a softer spectrum both in terms of E_{peak} and α due to lower Doppler boost and superposition of spectra respectively, contrary to what is observed. On the other hand, in case of a “top-hat” jet, hardly any high latitude emission is expected and the hard spectrum can survive even when observed close to the edge of the jet. The hard α then suggests subphotospheric dissipation to be the underlying emission mechanism. In this model Comptonisation can yield high polarisation since orthogonal Thomson scattering in the rest frame dominates near the edge of the jet. In contrast, regardless of the geometry, Jitter radiation cannot produce the observed high level of polarisation near the spectral peak.

In our current analysis, a spectral cutoff is observed beyond 2 MeV. By using the argument of $\gamma - \gamma$ attenuation (Lithwick & Sari 2001), we can constrain the lower limit of Lorentz factor of the outflow for the first and second episodes to be $\geq 78 \pm 23$ and 74 ± 23 respectively. This in turn gives an upper limit on the beaming angle for the first episode (second episode), $1/\Gamma \leq 0.73 \pm 0.22$ degrees (0.77 ± 0.24 degrees). This value is consistent with the viewing angle geometry (θ_v/θ_j) suggested by Waxman (2003). Alternatively, under the assumption of a narrow jet, the jet opening angle is inferred to be $\theta_j \sim 1/\Gamma \sim 1^\circ$,

similar to the lowest θ_j deduced from jet breaks observed in afterglows (Racusin et al. 2009).

Thus, combining the spectral analysis and the polarisation measurements, we deem it the most likely that the observed emission from GRB 160802A is due to subphotospheric dissipation taking place within a narrow GRB jet viewed along its boundary, with jet emissivity dropping sharply away from its edge.

To summarize, the spectral and timing properties are rich sources of information about emission mechanisms. Polarization of the prompt emission helped us to further narrow down the emission mechanisms. It also helped us to infer the jet geometry as high polarization is observed in case of this GRB. However, by the combined constraints given by spectro-polarimetric properties we need a narrow jet viewed along its edge. It is, however, on our radar to see in future for similar bright bursts whether we obtain a high polarization always by geometric effects only. Observation of afterglows is also a deciding factor as then we can measure the jet opening angles and even rule out such geometries when coupled with harder values of low energy spectral indices.

ACKNOWLEDGEMENTS

This research has made use of data obtained through the HEASARC Online Service, provided by the NASA/GSFC, in support of NASA High Energy Astrophysics Programs. This publication also uses the data from the AstroSat mission of the Indian Space Research Organisation (ISRO), archived at the Indian Space Science Data Centre (ISSDC). CZT-Imager is built by a consortium of Institutes across India including Tata Institute of Fundamental Research, Mumbai, Vikram Sarabhai Space Centre, Thiruvananthapuram, ISRO Satellite Centre, Bengaluru, Inter University Centre for Astronomy and Astrophysics, Pune, Physical Research Laboratory, Ahmedabad, Space Application Centre, Ahmedabad: contributions from the vast technical team from all these institutes are gratefully acknowledged.

REFERENCES

- Abdo, A. A., Ackermann, M., Ajello, M., et al. 2009, *ApJL*, 706, L138
 Ackermann, M., Asano, K., Atwood, W. B., et al. 2010, *ApJ*, 716, 1178
 Ackermann, M., Ajello, M., Asano, K., et al. 2013, *ApJS*, 209, 11
 Aharonian, F. A., Belyanin, A. A., Derishev, E. V., Kocharovsky, V. V., & Kocharovsky, V. V. 2002, *Phys. Rev. D*, 66, 023005
 Arnaud, K. A. 1996, in *Astronomical Society of the Pacific Conference Series*, Vol. 101, *Astronomical Data Analysis Software and Systems V*, ed. G. H. Jacoby & J. Barnes, 17
 Atwood, W. B., Abdo, A. A., Ackermann, M., et al. 2009, *ApJ*, 697, 1071
 Band, D., Matteson, J., Ford, L., et al. 1993, *ApJ*, 413, 281
 Basak, R., Iyyani, S., Chand, V., et al. 2017, *MNRAS*, 472, 891

Table 1: Summary of spectral fitting for the two emission episodes in GRB 160802A

Episode 1: (0 – 7 s)				
Parameters ^a	B	BB+B	CPL	BB+ CPL
α	$-0.52^{+0.04}_{-0.03}$	$-0.73^{+0.06}_{-0.05}$	–	–
β	$-2.6^{+0.1}_{-0.1}$	$-3.8^{+0.7}_{-\infty}$	–	–
E_p (keV)	297^{+15}_{-14}	429^{+37}_{-36}	–	–
E_c (MeV)	–	–	247^{+13}_{-12}	348^{+41}_{-34}
kT_{BB} (keV)	–	35^{+3}_{-4}	–	35^{+3}_{-3}
Γ_c	–	–	$0.60^{+0.03}_{-0.03}$	$0.70^{+0.05}_{-0.05}$
Flux ^b	7.7	8.0	7.9	8.0
pgstat/dof/BIC	395/341/430	367/339/414	435/342/464	368/340/409
$\Delta(\text{BIC})^c$	–	16	–	55
Episode 2: 15 – 20 s				
α	$-0.78^{+0.11}_{-0.11}$	$-1.1^{+0.2}_{-0.1}$	–	–
β	$-2.4^{+0.1}_{-0.2}$	$-3.8^{+3.0}_{-\infty}$	–	–
E_p (keV)	122^{+17}_{-13}	267^{+74}_{-86}	–	–
E_c (MeV)	–	–	173^{+24}_{-20}	326^{+139}_{-83}
kT_{BB} (keV)	–	17^{+3}_{-4}	–	17^{+3}_{-3}
Γ_c	–	–	$1.00^{+0.06}_{-0.06}$	$1.2^{+0.1}_{-0.1}$
Flux ^b	2.3	2.4	2.2	2.4
pgstat/dof/BIC	399/341/434	393/339/440	423/342/458	393/340/434
$\Delta(\text{BIC})^c$	–	-6	–	24

^aParameters are α , β and E_p for Band (B) model, kT_{BB} for the black body (BB) model, cut-off energy, E_c , and index Γ_c for the cut-off power law (CPL) model.

^bFlux in the units of 10^{-6} erg cm⁻² in 8 - 1000 keV.

^c ΔBIC is the decrease in BIC with respect to the Band model or the CPL model.

- Basak, R., & Rao, A. R. 2015, ApJ, 812, 156
Beloborodov, A. M. 2010, MNRAS, 407, 1033
Bhalerao, V., Kumar, V., Bhattacharya, D., Rao, A. R., & Vadawale, S. 2016, GRB Coordinates Network, Circular Service, No. 19782, #1 (2016), 19782
Bhalerao, V., Bhattacharya, D., Vibhute, A., et al. 2017, Journal of Astrophysics and Astronomy, 38, 31
Bissaldi, E. 2016, GRB Coordinates Network, Circular Service, No. 19754, #1 (2016), 19754
Burgess, J. M., & Ryde, F. 2015, MNRAS, 447, 3087
Burgess, J. M., Ryde, F., & Yu, H.-F. 2015, MNRAS, 451, 1511
Chattopadhyay, T., Vadawale, S. V., Shanmugam, M., & Goyal, S. K. 2014, Astrophysical Journal Supplement, 212, 12
Chattopadhyay, T., Vadawale, S. V., Aarthy, E., et al. 2017, ArXiv e-prints, arXiv:1707.06595
Cohen, E., Katz, J. I., Piran, T., et al. 1997, ApJ, 488, 330
Crider, A., Liang, E. P., Smith, I. A., et al. 1997, ApJL, 479, L39
Gehrels, N., & Razzaque, S. 2013, Frontiers of Physics, 8, 661
Gehrels, N., Chincarini, G., Giommi, P., et al. 2004, ApJ, 611, 1005
Ghirlanda, G., Celotti, A., & Ghisellini, G. 2003, A&A, 406, 879
Goldstein, A., Preece, R. D., Malozzi, R. S., et al. 2013, ApJS, 208, 21
González, M. M., Dingus, B. L., Kaneko, Y., et al. 2003, Nature, 424, 749
Guiriec, S., Gonzalez, M. M., Sacahui, J. R., et al. 2016, ApJ, 819, 79
Guiriec, S., Mochkovitch, R., Piran, T., et al. 2015a, ApJ, 814, 10
Guiriec, S., Connaughton, V., Briggs, M. S., et al. 2011, ApJL, 727, L33
Guiriec, S., Daigne, F., Hascoët, R., et al. 2013, ApJ, 770, 32
Guiriec, S., Kouveliotou, C., Daigne, F., et al. 2015b, ApJ, 807, 148
Izzo, L., Ruffini, R., Penacchioni, A. V., et al. 2012, A&A, 543, A10
Kaneko, Y., Preece, R. D., Briggs, M. S., et al. 2006, ApJS, 166, 298
Kass, R. E., & Rafferty, A. E. 1995, J. Am. Stat. Assoc., 90, 773
Katz, J. I. 1994, ApJL, 432, L107
Kelner, S. R., Aharonian, F. A., & Khangulyan, D. 2013, ApJ, 774, 61
Kouveliotou, C., Meegan, C. A., Fishman, G. J., et al. 1993, ApJL, 413, L101
Kozlova, A., Golenetskii, S., Aptekar, R., et al. 2016a, GRB Coordinates Network, Circular Service, No. 19535, #1 (2016), 19535
—. 2016b, GRB Coordinates Network, Circular Service, No. 19767, #1 (2016), 19767
Lithwick, Y., & Sari, R. 2001, ApJ, 555, 540
Lu, R.-J., Wei, J.-J., Liang, E.-W., et al. 2012, ApJ, 756, 112
Lundman, C., Pe'er, A., & Ryde, F. 2013, MNRAS, 428, 2430
Lundman, C., Vurm, I., & Beloborodov, A. M. 2016, ArXiv e-prints, arXiv:1611.01451
Medvedev, M. V. 2000, ApJ, 540, 704

Table 2: Spectral fit to GBM data in the coarse time intervals described in §3.4. Errors on the parameters are corresponding to a 90% confidence region.

Interval	Model	α Γ_1	β Γ_2	E_p E_{break}	kT_{BB}	PGstat/dof/BIC	Prefered model
[s]				[keV]	[keV]		
<i>i</i> (0.0, 1.0)	B	$-0.42^{+0.05}_{-0.05}$	$-3.45^{+0.60}_{-\infty}$	546^{+38}_{-37}	—	386/343/409	Band/BB+Band
	BB+B	$-0.51^{+0.04}_{-0.04}$	$-3.0^{+9.2}_{-3.0}$	680^{+46}_{-66}	47^{+9}_{-9}	375/341/411	
	bknpower	$0.64^{+0.04}_{-0.04}$	$2.31^{+0.09}_{-0.09}$	274^{+21}_{-20}	—	469/343/492	
<i>ii</i> (1.0, 2.0)	B	$-0.21^{+0.06}_{-0.06}$	$-2.76^{+0.19}_{-0.28}$	307^{+19}_{-18}	—	360/345/383	Band/BB+Band
	BB+B	$-0.40^{+0.12}_{-0.12}$	$-3.5^{+0.6}_{-\infty}$	412^{+61}_{-49}	37^{+6}_{-7}	345/341/380	
	bknpower	$0.57^{+0.04}_{-0.04}$	$2.32^{+0.08}_{-0.07}$	178^{+11}_{-10}	—	446/343/469	
<i>iii</i> (2.0, 3.0)	B	$-0.31^{+0.10}_{-0.09}$	$-2.79^{+0.27}_{-0.49}$	213^{+18}_{-24}	—	402/345/426	Band
	BB+B	$-0.63^{+0.23}_{-0.16}$	$-4.34^{+1.55}_{-\infty}$	304^{+57}_{-67}	33^{+5}_{-6}	398/341/433	
	bknpower	$0.72^{+0.05}_{-0.05}$	$2.39^{+0.12}_{-0.11}$	136^{+11}_{-11}	—	426/343/450	
<i>iv</i> (3.0, 4.0)	B	$-0.6^{+0.2}_{-0.1}$	$-2.8^{+0.4}_{-2.5}$	192^{+26}_{-30}	—	387/345/410	Band/bknpower
	BB + B	$-0.81^{+0.21}_{-0.21}$	$-3.26^{+0.85}_{-\infty}$	258^{+90}_{-43}	26^{+7}_{-7}	383/341/418	
	bknpower	$0.90^{+0.07}_{-0.07}$	$2.21^{+0.12}_{-0.10}$	104^{+12}_{-10}	—	341/343/414	
<i>v</i> (4.0, 5.0)	B	$-0.76^{+0.20}_{-0.20}$	$-2.48^{+0.28}_{-\infty}$	133^{+37}_{-23}	—	338/345/362	Band
	BB + B	$-1.05^{+1.78}_{-0.29}$	$-2.94^{+0.94}_{-\infty}$	190^{+121}_{-123}	21^{+71}_{-21}	337/343/372	
	bknpower	$1.12^{+0.09}_{-0.17}$	$2.32^{+0.24}_{-0.25}$	94^{+19}_{-26}	—	341/343/364	
<i>vi</i> (5.0, 6.0)	B	$-0.76^{+0.08}_{-0.08}$	$-9.36^{+6.64}_{-\infty}$	252^{+25}_{-31}	—	414/345/437	Band
	BB + B	$-0.95^{+0.21}_{-0.20}$	$-10^{+0}_{-\infty}$	304^{+109}_{-74}	36^{+74}_{-36}	411/343/446	
	bknpower	$1.00^{+0.06}_{-0.06}$	$2.44^{+0.26}_{-0.16}$	151^{+27}_{-17}	—	421/343/444	
<i>vii</i> (6.0, 7.0)	B	$-0.17^{+1.83}_{-0.80}$	$-2.13^{+0.23}_{-0.45}$	58^{+35}_{-21}	—	323/345/347	Band/bknpower
	BB + B	$0.28^{+\infty}_{-1.72}$	$-1.90^{+0.28}_{-0.54}$	38^{+181}_{-21}	$17^{+\infty}_{-17}$	323/343/358	
	bknpower	$0.72^{+0.57}_{-0.58}$	$2.06^{+0.35}_{-0.18}$	36^{+31}_{-8}	—	324/343/348	
<i>viii</i> (15.0, 17.0)	B	$-0.60^{+0.12}_{-0.11}$	$-2.22^{+0.10}_{-0.13}$	143^{+19}_{-16}	—	389/345/413	Band/BB+Band
	BB + B	$-0.96^{+0.14}_{-0.13}$	$-2.74^{+0.36}_{-\infty}$	280^{+79}_{-57}	19^{+3}_{-3}	375/343/410	
	bknpower	$1.00^{+0.05}_{-0.06}$	$2.12^{+0.07}_{-0.06}$	88^{+8}_{-8}	—	410/343/432	
<i>ix</i> (17.0, 18.0)	B	$-1.0^{+0.7}_{-0.3}$	$-2.4^{+0.3}_{-0.6}$	65^{+18}_{-23}	—	364/345/387	Band/bknpower
	BB + B	$1.2^{+\infty}_{-1.4}$	$-2.1^{+0.1}_{-0.2}$	24^{+22}_{-6}	20^{+6}_{-5}	359/343/394	
	bknpower	$1.40^{+0.15}_{-0.36}$	$2.32^{+0.25}_{-0.22}$	53^{+23}_{-20}	—	394/343/391	

Table 3: Detailed time-resolved Spectral fitting

Sr. no.	(t_1, t_2)	kT_{BB}	α	β	E_p (keV)	PGSTAT/dof/BIC	Preferred model
			Γ_1	Γ_2	E_{break}		
1	(-0.26, 0.32)	4.3 $^{+3.0}_{-4.3}$	-0.55 $^{+0.05}_{-0.09}$	-5.0 $^{+2.0}_{-\infty}$	951 $^{+168}_{-127}$	343/343/366	Band/bknpower
			-0.40 $^{+0.17}_{-0.15}$	-10 $^{+20}_{-\infty}$	850 $^{+9055}_{-115}$	335/341/370	
			0.84 $^{+0.05}_{-0.05}$	7 $^{+\infty}_{-3}$	1020 $^{+135}_{-188}$	341/343/364	
2	(0.32, 0.48)	48 $^{+460}_{-48}$	-0.41 $^{+0.08}_{-0.08}$	-8.0 $^{+5.0}_{-\infty}$	685 $^{+84}_{-71}$	325/343/349	Band
			-0.43 $^{+0.14}_{-0.15}$	-10 $^{+20}_{-\infty}$	746 $^{+167}_{-78}$	324/341/359	
			0.72 $^{+0.06}_{-0.19}$	2.9 $^{+0.6}_{-0.7}$	504 $^{+106}_{-212}$	353/343/376	
3	(0.48, 0.64)	47 $^{+21}_{-20}$	-0.36 $^{+0.13}_{-0.12}$	-3.4 $^{+0.8}_{-\infty}$	491 $^{+74}_{-62}$	357/343/381	Band
			-0.5 $^{+0.2}_{-0.2}$	-9.4 $^{+9.5}_{-\infty}$	586 $^{+142}_{-123}$	352/341/388	
			0.64 $^{+0.08}_{-0.13}$	2.4 $^{+0.3}_{-0.3}$	278 $^{+45}_{-72}$	374/343/398	
4	(0.64, 0.83)	25 $^{+26}_{-11}$	-0.20 $^{+0.17}_{-0.15}$	-3.36 $^{+0.80}_{-\infty}$	326 $^{+48}_{-44}$	318/343/341	Band
			-0.18 $^{+0.54}_{-0.27}$	-6 $^{+16}_{-\infty}$	372 $^{+79}_{-58}$	315/341/350	
			0.61 $^{+0.10}_{-0.18}$	2.5 $^{+0.4}_{-0.4}$	213 $^{+48}_{-58}$	339/343/362	
5	(0.83, 0.98)	17 $^{+7}_{-6}$	-0.02 $^{+0.22}_{-0.20}$	-2.34 $^{+0.20}_{-0.45}$	283 $^{+61}_{-41}$	412/343/435	Band
			1.8 $^{+\infty}_{-2.2}$	-2.3 $^{+0.2}_{-1.1}$	245 $^{+166}_{-40}$	408/341/443	
			0.50 $^{+0.10}_{-0.11}$	2.2 $^{+0.2}_{-0.2}$	181 $^{+23}_{-25}$	421/343/444	
6	(0.98, 1.1)	18 $^{+23}_{-5}$	-0.03 $^{+0.20}_{-0.18}$	-2.36 $^{+0.20}_{-0.33}$	316 $^{+55}_{-46}$	368/343/392	Band
			0.5 $^{+4.0}_{-1.0}$	-2.4 $^{+0.2}_{-1.1}$	314 $^{+450}_{-78}$	365/341/400	
			0.40 $^{+0.11}_{-0.12}$	2.2 $^{+0.2}_{-0.1}$	181 $^{+30}_{-25}$	382/343/405	
7	(1.1, 1.2)	8 $^{+\infty}_{-8}$	-0.16 $^{+0.48}_{-0.21}$	-2.82 $^{+0.38}_{-1.06}$	372 $^{+90}_{-55}$	310/343/333	Band
			-0.15 $^{+0.50}_{-0.60}$	-2.8 $^{+0.4}_{-0.9}$	361 $^{+322}_{-55}$	310/341/345	
			0.6 $^{+0.1}_{-0.1}$	2.4 $^{+0.2}_{-0.2}$	226 $^{+38}_{-35}$	321/343/344	
8	(1.2, 1.3)	29 $^{+13}_{-14}$	-0.11 $^{+0.20}_{-0.17}$	-2.63 $^{+0.32}_{-0.80}$	290 $^{+48}_{-42}$	333/343/356	Band
			-0.2 $^{+0.7}_{-0.3}$	-3.3 $^{+0.9}_{-\infty}$	401 $^{+125}_{-120}$	329/341/364	
			0.4 $^{+0.2}_{-0.1}$	2.2 $^{+0.2}_{-0.1}$	145 $^{+42}_{-16}$	352/343/375	
9	(1.3, 1.5)	37 $^{+13}_{-12}$	-0.20 $^{+0.17}_{-0.13}$	-3.3 $^{+0.7}_{-\infty}$	345 $^{+39}_{-48}$	364/343/388	Band
			-0.30 $^{+0.24}_{-0.23}$	-3.6 $^{+1.0}_{-\infty}$	427 $^{+126}_{-78}$	360/341/395	
			0.5 $^{+0.1}_{-0.1}$	2.3 $^{+0.2}_{-0.2}$	175 $^{+27}_{-23}$	379/343/402	
10	(1.5, 1.6)	38 $^{+15}_{-16}$	-0.23 $^{+0.18}_{-0.13}$	-3.4 $^{+0.9}_{-\infty}$	364 $^{+45}_{-56}$	315/343/338	Band
			-0.34 $^{+0.26}_{-0.23}$	-10 $^{+0}_{-\infty}$	455 $^{+128}_{-75}$	311/341/346	
			0.50 $^{+0.15}_{-0.12}$	2.3 $^{+0.3}_{-0.2}$	183 $^{+55}_{-25}$	333/343/356	
11	(1.6, 1.72)	13 $^{+37}_{-8}$	-0.36 $^{+0.18}_{-0.19}$	-3.2 $^{+0.8}_{-\infty}$	288 $^{+50}_{-47}$	309/343/332	Band
			-0.1 $^{+1.6}_{-0.6}$	-3.2 $^{+0.8}_{-\infty}$	288 $^{+117}_{-76}$	306/341/341	
			0.72 $^{+0.08}_{-0.09}$	2.5 $^{+0.3}_{-0.2}$	186 $^{+26}_{-30}$	321/343/344	
12	(1.72, 1.9)	41 $^{+8}_{-6}$	-0.3 $^{+0.2}_{-0.2}$	-3.5 $^{+0.9}_{-\infty}$	250 $^{+37}_{-34}$	348/343/371	Band
			-0.5 $^{+0.5}_{-0.3}$	-10 $^{+0}_{-\infty}$	306 $^{+93}_{-49}$	346/341/381	
			0.68 $^{+0.11}_{-0.15}$	2.5 $^{+0.4}_{-0.3}$	157 $^{+36}_{-31}$	355/343/378	
13	(1.9, 2.05)	41 $^{+7}_{-7}$	-0.12 $^{+0.21}_{-0.18}$	-2.8 $^{+0.4}_{-1.2}$	236 $^{+35}_{-32}$	337/343/360	Band/bknpower
			-0.7 $^{+0.3}_{-0.3}$	-10 $^{+0}_{-\infty}$	438 $^{+241}_{-122}$	333/341/368	
			0.5 $^{+0.1}_{-0.1}$	2.4 $^{+0.2}_{-0.2}$	142 $^{+19}_{-15}$	336/343/359	
14	(2.05, 2.2)	32 $^{+7}_{-8}$	-0.06 $^{+0.20}_{-0.20}$	-2.4 $^{+0.2}_{-0.4}$	216 $^{+43}_{-32}$	319/343/342	Band
			-0.5 $^{+0.3}_{-0.2}$	-3.5 $^{+1.1}_{-\infty}$	402 $^{+149}_{-124}$	315/341/350	
			0.52 $^{+0.12}_{-0.14}$	2.2 $^{+0.2}_{-0.1}$	129 $^{+24}_{-19}$	326/343/350	
15	(2.2, 2.4)	60 $^{+\infty}_{-60}$	-0.37 $^{+0.18}_{-0.15}$	-3.0 $^{+0.5}_{-\infty}$	225 $^{+34}_{-30}$	332/343/355	Band
			-0.1 $^{+4.7}_{-0.9}$	-2.1 $^{+0.3}_{-1.6}$	95 $^{+211}_{-41}$	331/341/366	
			0.82 $^{+0.08}_{-0.12}$	2.7 $^{+0.4}_{-0.4}$	173 $^{+26}_{-37}$	338/343/361	
16	(2.4, 2.74)	27 $^{+\infty}_{-22}$	-0.2 $^{+0.2}_{-0.2}$	-2.8 $^{+0.4}_{-\infty}$	181 $^{+34}_{-26}$	413/343/436	Band
			-0.50 $^{+2.42}_{-0.37}$	-9.4 $^{+7.1}_{-\infty}$	246 $^{+88}_{-87}$	412/341/447	
			0.64 $^{+0.13}_{-0.12}$	2.3 $^{+0.3}_{-0.2}$	109 $^{+27}_{-12}$	421/343/444	
17	(2.74, 3)	31 $^{+\infty}_{-20}$	-0.51 $^{+0.22}_{-0.16}$	-3.40 $^{+1.0}_{-\infty}$	214 $^{+36}_{-40}$	356/343/380	Band
			-0.8 $^{+0.2}_{-0.3}$	-10 $^{+0}_{-\infty}$	279 $^{+146}_{-27}$	354/341/389	
			0.9 $^{+0.1}_{-0.1}$	2.5 $^{+0.4}_{-0.3}$	142 $^{+32}_{-26}$	362/343/386	

Table 3: Detailed time-resolved Spectral fitting (continued)

Sr. no.	(t_1, t_2)	kT_{BB}	α	β	E_p (keV)	PGSTAT/dof/BIC	Preferred model
			Γ_1	Γ_2	E_{break}		
18	(3, 3.45)	$27^{+\infty}_{-16}$	$-0.60^{+0.24}_{-0.20}$	$-2.5^{+0.3}_{-\infty}$	155^{+41}_{-30}	379/343/402	Band/bknpower
			$-1.0^{+0.6}_{-0.4}$	$-2.6^{+0.7}_{-\infty}$	231^{+309}_{-166}	378/341/413	
			$1.0^{+0.1}_{-0.1}$	$2.3^{+0.2}_{-0.2}$	103^{+20}_{-16}	378/343/401	
19	(3.45, 3.86)	$21^{+\infty}_{-21}$	$-0.51^{+0.15}_{-0.14}$	$-10^{+20}_{-\infty}$	204^{+21}_{-20}	407/343/430	Band
			$-0.55^{+0.30}_{-0.30}$	$-10^{+0}_{-\infty}$	224^{+70}_{-36}	405/341/441	
			$0.80^{+0.14}_{-0.13}$	$2.3^{+0.4}_{-0.2}$	107^{+38}_{-15}	418/343/441	
20	(3.86, 4.2)	$29^{+\infty}_{-16}$	$-0.6^{+0.2}_{-0.1}$	$-2.8^{+0.5}_{-\infty}$	204^{+38}_{-36}	321/343/345	Band/bknpower
			$-0.8^{+0.8}_{-0.5}$	$-2.8^{+0.9}_{-\infty}$	235^{+337}_{-171}	321/341/356	
			$0.9^{+0.1}_{-0.1}$	$2.24^{+0.29}_{-0.18}$	115^{+32}_{-20}	325/343/348	
21	(4.2, 5)	69^{+408}_{-69}	$-0.75^{+0.26}_{-0.22}$	$-2.38^{+0.25}_{-\infty}$	111^{+28}_{-30}	368/343/391	Band/bknpower
			$3.7^{+\infty}_{-4.7}$	$-2.2^{+0.2}_{-0.3}$	75^{+75}_{-9}	367/341/402	
			$1.1^{+0.1}_{-0.1}$	$2.2^{+0.3}_{-0.1}$	72^{+25}_{-10}	368/343/391	
22	(5, 5.4)	$39^{+\infty}_{-9}$	$-0.6^{+0.1}_{-0.1}$	$-9.2^{+\infty}_{-\infty}$	246^{+35}_{-19}	366/343/390	Band/bknpower
			$-1.0^{+0.7}_{-0.3}$	$-10^{+0}_{-\infty}$	338^{+186}_{-107}	364/341/399	
			$0.91^{+0.08}_{-0.09}$	$2.5^{+0.3}_{-0.2}$	152^{+26}_{-21}	367/343/391	
23	(5.4, 5.6)	$27^{+\infty}_{-27}$	$-0.60^{+0.10}_{-0.12}$	$-3.5^{+0.9}_{-\infty}$	277^{+43}_{-35}	369/343/392	Band
			$-0.58^{+0.35}_{-0.32}$	$-3.61^{+0.9}_{-\infty}$	282^{+123}_{-46}	369/341/404	
			$0.90^{+0.08}_{-0.08}$	$2.6^{+0.3}_{-0.3}$	184^{+30}_{-31}	377/343/401	
24	(15.7, 15.9)	22^{+10}_{-8}	$-0.40^{+0.24}_{-0.17}$	$-2.3^{+0.3}_{-0.5}$	247^{+56}_{-54}	340/343/363	Band
			$-0.48^{+0.47}_{-0.30}$	$-2.6^{+0.4}_{-\infty}$	347^{+179}_{-100}	335/341/370	
			$0.62^{+0.20}_{-0.14}$	$2.0^{+0.3}_{-0.1}$	109^{+55}_{-15}	351/343/374	
25	(15.9, 16.0)	27^{+7}_{-8}	$-0.48^{+0.25}_{-0.17}$	$-2.9^{+0.5}_{-\infty}$	191^{+36}_{-38}	337/343/360	Band/bknpower
			$-0.8^{+0.3}_{-0.3}$	$-4.4^{+2.0}_{-\infty}$	289^{+136}_{-91}	333/341/369	
			$0.76^{+0.11}_{-0.11}$	$2.3^{+0.2}_{-0.1}$	104^{+15}_{-11}	337/343/360	
26	(16.0, 16.15)	48^{+81}_{-12}	$-0.36^{+0.40}_{-0.26}$	$-2.40^{+0.25}_{-0.51}$	127^{+32}_{-29}	338/343/362	Band/bknpower
			$-0.07^{+0.50}_{-0.90}$	$-2.2^{+0.2}_{-0.4}$	86^{+191}_{-22}	336/341/371	
			$0.76^{+0.13}_{-0.15}$	$2.18^{+0.14}_{-0.12}$	75^{+11}_{-10}	340/343/363	
27	(16.15, 16.3)	$15^{+4.3}_{-3.3}$	$-0.2^{+0.4}_{-0.3}$	$-2.4^{+0.2}_{-0.3}$	102^{+20}_{-20}	332/343/356	Band
			$-0.7^{+0.1}_{-0.3}$	$-10^{+0}_{-\infty}$	214^{+15}_{-30}	329/341/364	
			$1.1^{+0.1}_{-0.1}$	$2.2^{+0.3}_{-0.1}$	72^{+25}_{-10}	368/343/365	
28	(16.3, 16.5)	$78^{+\infty}_{-51}$	$-0.6^{+0.3}_{-0.2}$	$-2.5^{+0.2}_{-0.5}$	99^{+21}_{-16}	281/343/305	Band/bknpower
			$-0.5^{+0.4}_{-0.2}$	$-3.4^{+1.1}_{-\infty}$	82^{+25}_{-18}	281/343/316	
			$1.15^{+0.11}_{-0.14}$	$2.5^{+0.3}_{-0.2}$	86^{+17}_{-18}	286/343/310	
29	(16.5, 16.9)	$8.5^{+\infty}_{-8.5}$	$-0.6^{+0.3}_{-0.2}$	$-2.5^{+0.3}_{-0.4}$	86^{+14}_{-13}	356/343/379	Band/bknpower
			$-0.6^{+1.8}_{-0.8}$	$-2.6^{+0.5}_{-\infty}$	106^{+137}_{-23}	355/341/390	
			$1.15^{+0.11}_{-0.14}$	$2.5^{+0.3}_{-0.2}$	86^{+17}_{-18}	286/343/380	
30	(16.9, 17.6)	$5^{+1.7}_{-5}$	$-1.0^{+0.3}_{-0.2}$	$-2.6^{+0.3}_{-1.4}$	72^{+17}_{-14}	367/343/390	Band/bknpower
			$0.9^{+\infty}_{-1.9}$	$-2.5^{+0.2}_{-0.4}$	82^{+17}_{-13}	365/341/400	
			$1.15^{+0.11}_{-0.14}$	$2.5^{+0.3}_{-0.2}$	86^{+17}_{-18}	286/343/394	
31	(17.6, 20.34)	5^{+6}_{-5}	$0.05^{+2.30}_{-1.01}$	$-2.4^{+0.3}_{-0.6}$	36^{+15}_{-11}	276/343/299	bknpower
			$-0.5^{+5.0}_{-0.8}$	$-2.7^{+0.3}_{-1.4}$	78^{+24}_{-17}	273/341/308	
			$1.15^{+0.11}_{-0.14}$	$2.5^{+0.3}_{-0.2}$	86^{+17}_{-18}	286/343/302	

- Meegan, C., Lichti, G., Bhat, P. N., et al. 2009, *ApJ*, 702, 791
- Meszaros, P., & Rees, M. J. 1993, *ApJ*, 405, 278
- Page, K. L., Starling, R. L. C., Fitzpatrick, G., et al. 2011, *MNRAS*, 416, 2078
- Panasjuk, M. I., Svertilov, S. I., Bogomolov, V. V., et al. 2016, GRB Coordinates Network, Circular Service, No. 19759, (2016), 19759
- Pe'er, A. 2008, *ApJ*, 682, 463
- Preece, R. D., Briggs, M. S., Mallozzi, R. S., et al. 1998, *ApJL*, 506, L23
- Prosekin, A. Y., Kelner, S. R., & Aharonian, F. A. 2016, *ArXiv e-prints*, arXiv:1607.01522
- Racusin, J. L., Liang, E. W., Burrows, D. N., et al. 2009, *ApJ*, 698, 43
- Rees, M. J., & Meszaros, P. 1992, *MNRAS*, 258, 41P
- . 1994, *ApJL*, 430, L93
- Ryde, F. 2005, *ApJL*, 625, L95
- Ryde, F., & Svensson, R. 1999, *Astrophysical Letters and Communications*, 39, 285
- Sari, R., Narayan, R., & Piran, T. 1996, *ApJ*, 473, 204
- Sari, R., & Piran, T. 1997, *MNRAS*, 287, 110
- Sari, R., Piran, T., & Narayan, R. 1998, *ApJL*, 497, L17
- Scargle, J. D., Norris, J. P., Jackson, B., & Chiang, J. 2013, *ApJ*, 764, 167
- Schwarz, G. 1995, *AnSta*, 6, 461
- Singh, K. P., Tandon, S. N., Agrawal, P. C., et al. 2014, in *Society of Photo-Optical Instrumentation Engineers (SPIE) Conference Series*, Vol. 9144, Society of Photo-Optical Instrumentation Engineers (SPIE) Conference Series
- Tamura, T., Yoshida, A., Sakamoto, T., et al. 2016, GRB Coordinates Network, Circular Service, No. 19778, #1 (2016), 19778
- Tavani, M. 1996, *ApJ*, 466, 768
- Uhm, Z. L., & Zhang, B. 2014, *Nature Physics*, 10, 351
- Vadawale, S. V., Chattopadhyay, T., Rao, A. R., et al. 2015, *Astronomy & Astrophysics*, 578, 73
- Vianello, G., Gill, R., Granot, J., et al. 2017, *ArXiv e-prints*, arXiv:1706.01481
- Wang, Y.-Z., Wang, H., Zhang, S., et al. 2017, *ApJ*, 836, 81
- Waxman, E. 2003, *Nature*, 423, 388